Materials Horizons

ROYAL SOCIETY OF CHEMISTRY

COMMUNICATION

View Article Online
View Journal | View Issue

Cite this: *Mater. Horiz.*, 2026, **13**, 2946

Received 8th July 2025,
Accepted 5th January 2026

DOI: 10.1039/d5mh01295c

rsc.li/materials-horizons

Liquid crystal elastomer-based reversible metamorphosis for loss-less droplet manipulation

Adil Majeed Rather, Sreekiran Pillai, Abhigith Nair, Mohammad Javad Zarei, Young Jae Kim, Huiqin Ni and Arun Kumar Kota *

Liquid crystal elastomers (LCEs) are a class of smart materials that combine the anisotropic properties of liquid crystals with the elasticity of polymers, enabling reversible metamorphosis (*i.e.*, shape transformation) in response to external stimuli. This reversible metamorphosis makes them ideal for many applications including soft robotics, artificial muscles, sensors, actuators, responsive coatings, *etc.* Prior studies have designed LCE surfaces with superhydrophobicity (*i.e.*, extreme repellency to high surface tension liquid like water), but the combination of reversible metamorphosis of LCEs with superomniphobicity (*i.e.*, extreme repellency to both high and low surface tension liquids) is unexplored. In this work, we developed LCE-based superomniphobic surfaces with reversible metamorphosis by laser texturing followed by low surface energy surface modification. Our LCE-based superomniphobic surfaces display extreme repellence to both aqueous and organic liquids as well as reversible metamorphosis due to nematic–isotropic transition of LCE. Utilizing these properties, we demonstrated loss-less manipulation of aqueous and organic liquid droplets, enabling merging, mixing, chemical reaction and microfluidic gating. We envision that our LCE-based superomniphobic surfaces with reversible metamorphosis will pave the way towards a wide range of applications including microfluidic reactors, lab-on-chip technologies, adaptive liquid-handling devices, controlled drug delivery systems *etc.*

New concepts

This work introduces a novel class of reversible metamorphic superomniphobic surfaces based on liquid crystal elastomers (LCEs), uniquely combining thermally triggered shape morphing with superomniphobicity in a single, scalable material platform. By engineering laser-fabricated re-entrant textures alongside fluorinated surface modifications, these surfaces achieve unprecedented dual functionality, enabling loss-less, contamination-free, and reversible manipulation of aqueous and organic droplets, including merging, mixing, and selective chemical reactions. Furthermore, the surfaces demonstrate thermally controlled on–off droplet gating for microfluidic devices, while maintaining both their metamorphic and superomniphobic properties under harsh chemical, UV, and mechanical conditions. This synergistic integration of programmable shape change with robust superomniphobicity represents a transformative materials concept, paving the way for future adaptive lab-on-chip systems, responsive soft robotics, programmable liquid-handling devices, and dynamic anti-fouling coatings.

1. Introduction

Liquid crystal elastomers (LCEs) are a class of smart materials that combine the anisotropic properties of liquid crystals with the elasticity of polymers, enabling reversible metamorphosis (*i.e.*, shape transformation) in response to external stimuli.[1–5] This reversible metamorphosis makes them ideal for many applications including soft robotics,[6,7] artificial muscles,[8,9] sensors,[10,11] actuators,[12,13] responsive coatings[14,15] *etc.* While the reversible metamorphosis of LCEs have been extensively explored, their integration with liquid repellency has received limited attention. Prior studies have designed LCE surfaces with superhydrophobicity (*i.e.*, extreme repellency to high surface tension liquid like water).[16–20] However, the combination of reversible metamorphosis of LCEs with superomniphobicity (*i.e.*, extreme repellency to both high and low surface tension liquids) is unexplored in the present literature. The integration of reversible metamorphosis and superomniphobicity into a single material is non-obvious and requires a rational design. Integrating reversible metamorphosis with superomniphobicity can lead to smart materials that have potential applications in microfluidic reactors, lab-on-chip technologies, adaptive liquid-handling devices, controlled drug delivery systems *etc.* So, in this work, we developed LCE-based superomniphobic surfaces with reversible metamorphosis using a simple, scalable and solvent-free CO_2 laser texturing process to obtain re-entrant texture, followed by surface modification to impart low solid surface energy. Our LCE-based superomniphobic surfaces are not only extremely repellent to both aqueous and organic liquids, but also display reversible metamorphosis due to nematic–isotropic transition[21–23] upon multiple heating–cooling

Department of Mechanical and Aerospace Engineering, North Carolina State University, Raleigh 27695, USA. E-mail: akota2@ncsu.edu

cycles. Utilizing this reversible metamorphosis of our LCE-based superomniphobic surfaces, we demonstrated loss-less manipulation of a wide variety of liquid droplets, enabling merging, mixing and chemical reaction, as well as microfluidic gating. This combination of reversible metamorphosis and superomniphobicity addresses the limitations of prior studies and opens new avenues for multifunctional smart materials in dynamic and chemically diverse environments.

In order to fabricate LCE-based superomniphobic surfaces, it is first important to have a good understanding of the fundamentals of wetting that lead to superomniphobicity. The primary measure of wetting of a liquid on a nontextured (*i.e.*, smooth) solid surface is the Young's contact angle θ.[24] When a liquid droplet comes into contact with a textured solid surface, it displays an apparent contact angle θ^*, which is different from the Young's contact angle θ. On the textured solid surface, the droplet can assume either the Wenzel state[25] or the Cassie–Baxter state.[26] In the Wenzel state, the liquid droplet completely penetrates the surface texture, while in the Cassie–Baxter state, there are pockets of air trapped within the surface texture beneath the droplet. The reduced solid–liquid contact area and the increased liquid–air contact area in the Cassie–Baxter state often allow droplets to display a very high apparent advancing and receding contact angles, θ^*_{adv} and θ^*_{rec}, as well as very low contact angle hysteresis $\Delta\theta^* = \theta^*_{adv} - \theta^*_{rec}$.[27–30] Such low contact angle hysteresis results in high mobility of the droplets with very low sliding angle ω (the minimum angle by which the surface must be tilted relative to the horizontal for the droplet to slide).[31] As a result, the Cassie–Baxter state is preferred for designing super-repellent surfaces with apparent contact angles $\theta^* > 150^\circ$ and sliding angles $\omega < 10^\circ$. Surfaces are considered superhydrophobic if they display $\theta^* > 150^\circ$ and $\omega < 10^\circ$ for high surface tension liquids (*e.g.*, water),[32–35] and superomniphobic if they display $\theta^* > 150^\circ$ and $\omega < 10^\circ$ for high surface tension liquids as well as low surface tension liquids (*e.g.*, hexadecane).[36,37] Unlike superhydrophobic surfaces, re-entrant texture (*e.g.*, convex, overhang or undercut texture) is necessary to design superomniphobic surfaces.[38] Many prior reports have demonstrated superomniphobicity through an appropriate combination of re-entrant texture and low solid surface energy.[39–43]

2. Results and discussion

Based on the above understanding, LCEs can be rendered superomniphobic by imparting re-entrant texture and low solid surface energy to its surface. We fabricated the LCE surfaces using a two-stage chemical reaction.[44,45] The first stage consisted of a base-catalyzed thiol-acrylate Michael addition reaction, followed by a second stage photochemical reaction between the residual acrylate groups (Fig. 1a). We used RM-257 (4-(3-Acryloyloxy- propyloxy)-benzoic acid 2-methyl-1,4-phenylene ester) as the liquid crystal monomer,

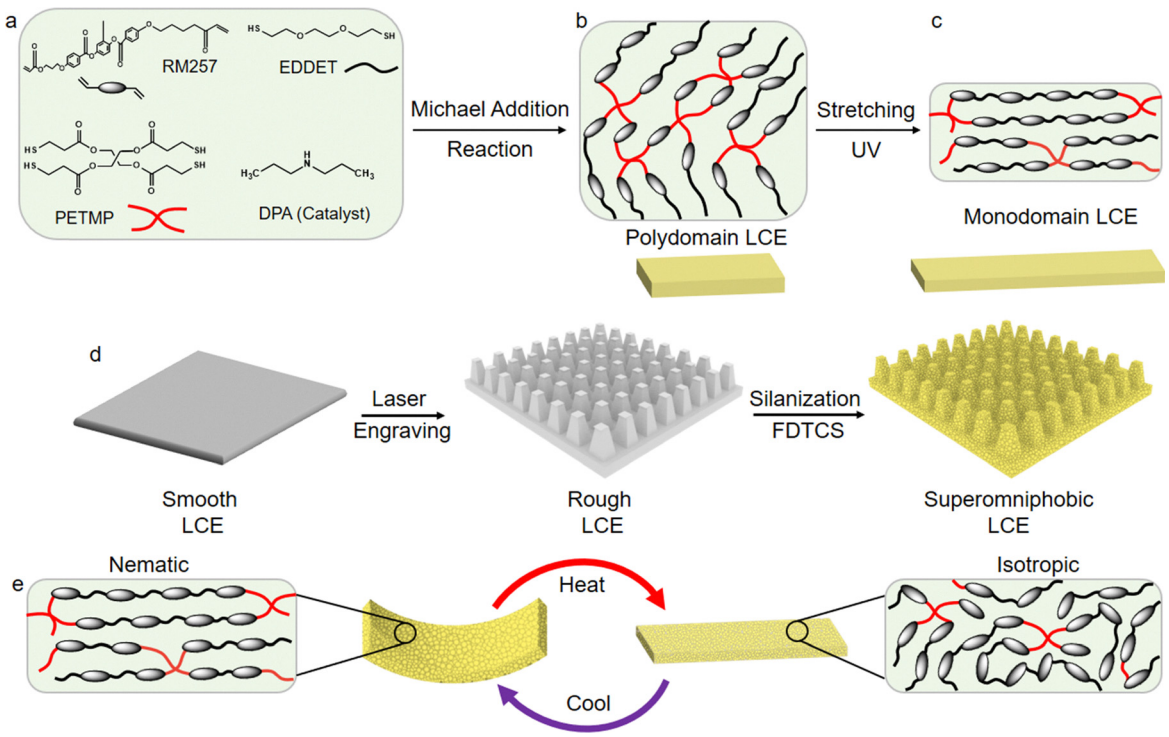

Fig. 1 Fabrication of LCE-based superomniphobic surfaces. (a) Chemical structures of liquid crystal monomer RM257, dithiol flexible spacer (EDDET), tetrafunctional thiol crosslinker (PETMP) and catalyst dipropylamine (DPA). (b) Schematic depicting the polydomain structure formed *via* thiol-acrylate Michael addition reaction. (c) Schematic depicting the monodomain structure formed after orienting the mesogens *via* mechanical stretching and UV cross-linking. (d) Designing re-entrant structures on LCE surfaces using laser texturing, followed by surface modification with a fluorinated silane FDTCS (heptadecafluoro-1,1,2,2-tetrahydrodecyl trichlorosilane). (e) Reversible metamorphosis of LCE-based superomniphobic surfaces due to nematic–isotropic transition.

EDDET (2,2-(ethylenedioxy) diethanethiol) as the spacer, PETMP (pentaerythritol tetrakis(3-mercaptopropionate)) as the crosslinker, DPA (dipropylamine) as the catalyst, and HHMP ((2-hydroxyethoxy)-2-methylpropiophenone) as the photoinitiator (see Experimental section). To confirm LCE formation, we characterized the chemical conversion of the monomer mixture into the crosslinked network using FTIR spectroscopy (see Experimental section). To fabricate superomniphobic LCE, in the first stage, the solution was cast into an LCE film, resulting in an opaque nematic polydomain structure.[46] In the second stage, the LCE film was stretched into the desired shape, and the residual acrylate groups were UV cross-linked, resulting in a transparent nematic monodomain structure.[47] Then, we fabricated micropillars with re-entrant texture on the LCE surface (solid surface energy, $\gamma_{sv} \approx 36$ mN m^{-1}; Fig. 1b and SI Section S1) using an inexpensive, solvent-free CO_2 laser ablation technique (see Experimental section). Then, we modified the re-entrant textured LCE surfaces with a fluorinated silane FDTCS (heptadecafluoro-1,1,2,2-tetrahydrodecyl trichlorosilane) to impart low solid surface energy ($\gamma_{sv} \approx 10$ mN m^{-1}).[39,41] The resulting fluorinated LCE surfaces displayed superomniphobicity as well as reversible metamorphosis due to nematic–isotropic transition (Fig. 1c).[21–23]

To better understand the fabricated LCE films, we characterized the chemical composition with Fourier Transform Infrared (FTIR) spectroscopy. Comparing the FTIR spectra of the individual components with the crosslinked LCE (Fig. 2a), we found that the characteristic acrylate peaks (C=C stretching at 1637 cm^{-1} and =C–H stretching at 3054 cm^{-1}) and the thiol S–H stretching peak at 2686 cm^{-1} disappeared after crosslinking, confirming the network formation (Fig. 2b–d).[48] Furthermore, we characterized the structural orientation of polydomain and monodomain LCEs with polarized light microscopy (Fig. 2e and f). The polydomain LCE transmitted light under all rotation angles, confirming randomly oriented LCE directors without preferential alignment. In contrast, the mechanically stretched monodomain LCE exhibited alternating bright and dark states at $\sim 45^\circ$ intervals relative to the polarizer axis, demonstrating successful alignment of the LCE directors.[49–51]

The key parameters influencing the surface texture (and hence superomniphobicity) were laser power and laser raster speed. Laser–material interactions are inherently complex and multidimensional with nonlinear parametric scaling, necessitating an iterative experimental optimization.[52–54] To systematically investigate the influence of laser power on the surface texture and surface wettability, we ablated the LCE film surface with different laser powers at a constant laser raster speed of 29 cm s^{-1} and subsequently modified the laser-ablated surfaces with the fluorinated silane. Then, we studied the surface wettability with water (surface tension, $\gamma_{lv} = 72.1$ mN m^{-1}) and hexadecane ($\gamma_{lv} = 27.5$ mN m^{-1}). As fabricated LCE surfaces were omniphilic ($\theta_{adv} = 72^\circ$ and $\theta_{rec} = 0^\circ$ for water, and $\theta_{adv} = 14^\circ$, $\theta_{rec} = 0^\circ$ for hexadecane; SI Section S2). When the LCE surface was subjected to laser ablation, the surface absorbed the laser energy,[55–57] and the complex laser–material interactions resulted in textured surfaces. As the laser power increased, the surface roughness increased, and resulted in enhanced liquid repellency (*i.e.*, higher contact angles and lower roll off angles) after surface fluorination to impart low solid surface energy. For example, at a low power of 1 W, micropillars developed on the LCE surfaces (Fig. 3a and SI Section S3). After surface fluorination, the micropillar LCE surfaces displayed superhydrophobicity, but not superomniphobicity ($\theta^*_{adv} = 155^\circ$, $\theta^*_{rec} = 150^\circ$, $\omega = 6^\circ$ for water, and $\theta^*_{adv} = 62^\circ$, $\theta^*_{rec} = 0^\circ$ and no sliding for hexadecane; Fig. 3c and d). This is because the micropillars did not develop re-entrant texture. While these micropillars resulted in the Cassie–Baxter state and effective repellency for high surface tension liquids (*e.g.*, water), the lack of sufficient re-entrant texture resulted in the Wenzel state and lack of effective repellency for low surface tension liquids (*e.g.*, hexadecane). As the laser power was increased to 6 W, the resulting LCE micropillars developed re-entrant texture (Fig. 3b and SI Section S3). As a result, after surface fluorination, the micropillar LCE surfaces displayed superomniphobicity ($\theta^*_{adv} = 163^\circ$, $\theta^*_{rec} = 159^\circ$, $\omega = 4^\circ$ for water, and $\theta^*_{adv} = 156^\circ$, $\theta^*_{rec} = 150^\circ$, $\omega = 7^\circ$ for hexadecane). The high contact angles and low roll off angles for water and hexadecane indicate that both the liquid droplets adopted the Cassie−Baxter state on the micropillar LCE surfaces. As the laser power was further increased to 12 W, the micropillar LCE surfaces continued to display superomniphobicity ($\theta^*_{adv} = 163^\circ$, $\theta^*_{rec} = 159^\circ$, $\omega = 4^\circ$ for water, and $\theta^*_{adv} = 157^\circ$, $\theta^*_{rec} = 151^\circ$, $\omega = 7^\circ$ for hexadecane; Fig. 3c and d). However, at significantly higher laser power (above 15 W), the LCE surfaces were damaged by the laser (cut or burnt; SI Section S4). Therefore, in this work, we choose a laser power of 6 W for fabricating LCE-based superomniphobic surfaces.

In addition to laser power, laser raster speed is another key parameter for designing superomniphobicity on LCE surfaces. To systematically investigate the influence of laser raster speed on texture and surface wettability, we ablated the surface of LCE with different laser raster speeds at constant laser power of 6 W and subsequently modified the surface with the fluorinated silane. At a high laser raster speed of 29 cm s^{-1} (the maximum power capability of the CO_2 laser system utilized in this study), the micropillar LCE surfaces displayed superomniphobicity ($\theta^*_{adv} = 164^\circ$, $\theta^*_{rec} = 160^\circ$, $\omega = 4^\circ$ for water, and $\theta^*_{adv} = 157^\circ$, $\theta^*_{rec} = 150^\circ$, $\omega = 7^\circ$ for hexadecane; Fig. 4c and d). As the laser raster speed decreased to $\sim$24 cm s^{-1}, the resulting LCE micropillars still developed re-entrant textures (Fig. 4a and SI Section S3). As a result, after surface fluorination, the micropillar LCE surfaces displayed superomniphobicity ($\theta^*_{adv} = 160^\circ$, $\theta^*_{rec} = 155^\circ$, $\omega = 4^\circ$ for water, and $\theta^*_{adv} = 156^\circ$, $\theta^*_{rec} = 150^\circ$, $\omega = 7^\circ$ for hexadecane; Fig. 4c and d). The high contact angles and low sliding angles for water and hexadecane indicate that both the liquid droplets adopted the Cassie−Baxter state on the micropillar LCE surfaces. At a low raster speed of 15 cm s^{-1}, micropillars developed on the LCE surfaces (Fig. 4b and SI Section S3). After surface fluorination, the micropillar LCE surfaces displayed superhydrophobicity, but not superomniphobicity ($\theta^*_{adv} = 157$, $\theta^*_{rec} = 151$, $\omega = 5^\circ$ for water, and $\theta^*_{adv} = 85^\circ$, $\theta^*_{rec} = 0^\circ$ and no sliding for hexadecane; Fig. 4c and d). This is because the re-entrant texture developed on micropillars was damaged due to prolonged laser exposure

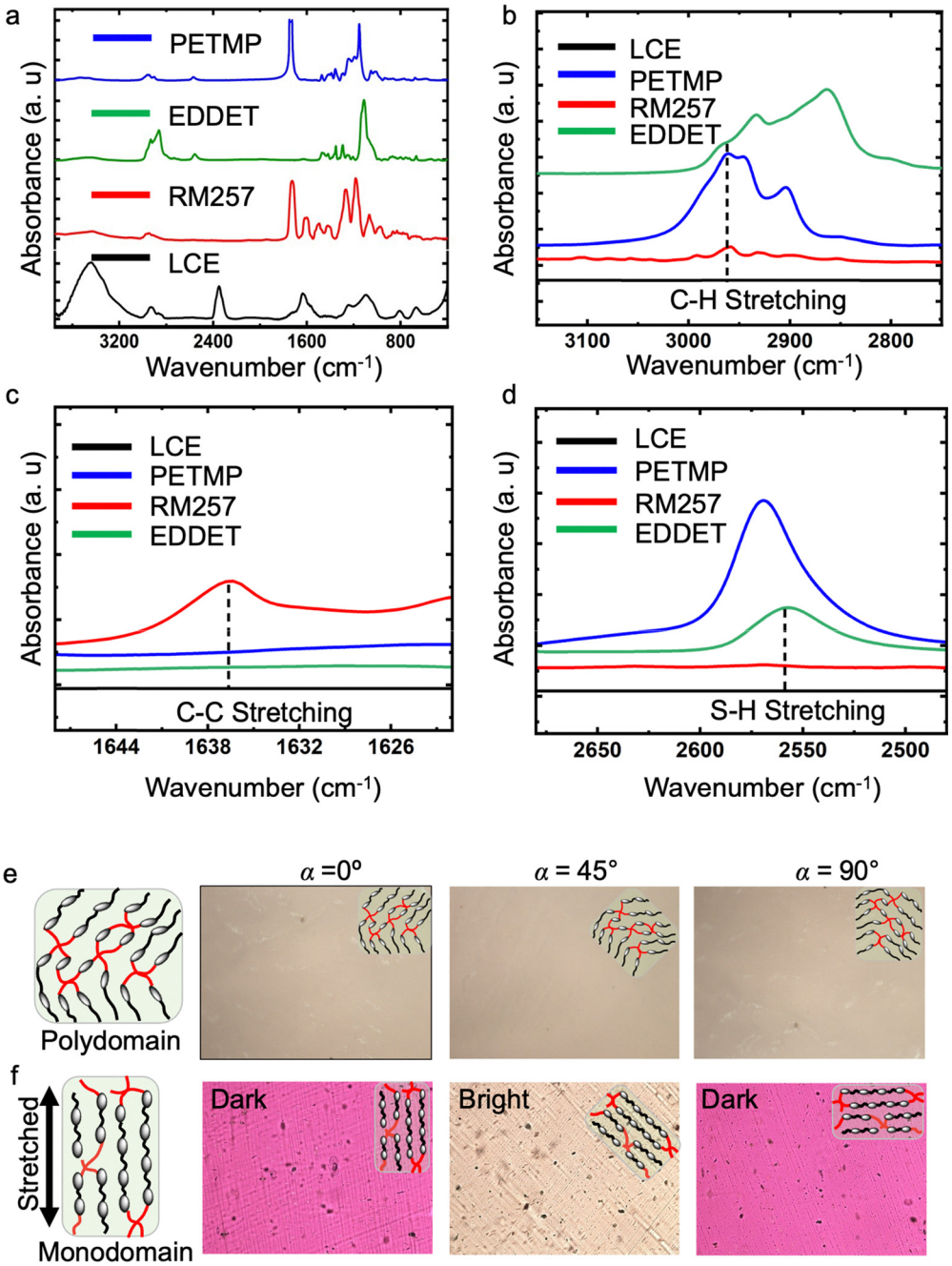

Fig. 2 Characterization of LCE. FTIR spectra of LCE components and crosslinked LCE. (b–d) FTIR spectra of LCE components and crosslinked LCE indicating disappearance of acrylate and thiol peaks after crosslinking. Polarized light microscopy of LCE in (a) polydomain structure and (b) monodomain structure.

at low raster speeds, leading to localized heating (or burning). As a result, while these micropillars resulted in the Cassie–Baxter state and effective repellency for high surface tension liquids (*e.g.*, water), the lack of re-entrant texture resulted in the Wenzel state and lack of effective repellency for low surface tension liquids (*e.g.*, hexadecane). As the laser raster speed was significantly reduced (below 15 cm s^{-1}), the LCE surfaces were damaged (SI Section S4). Therefore, in this work, we choose a laser raster speed of 24 cm s^{-1} for fabricating LCE-based superomniphobic surfaces.

The superomniphobicity of the micropillar LCE surfaces is not only due to the re-entrant texture obtained from laser ablation, but also due to the low solid surface energy obtained from the fluorinated silane, FDTCS. To study this, we characterized the surface chemistry of laser ablated LCE, before and after fluorination, with FTIR (see Experimental Section). A comparison of the FTIR spectra (Fig. 5a) of laser ablated LCE, before and after fluorination, confirms the presence of fluorocarbon functional groups (which impart low solid surface energy) after fluorination, with strong absorption peaks around

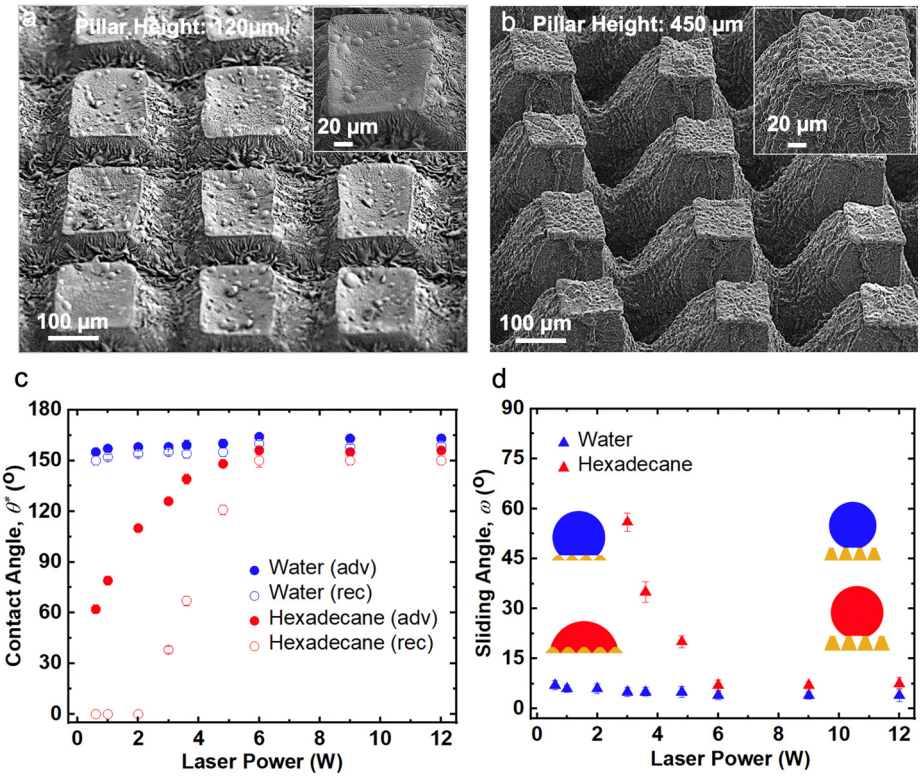

Fig. 3 Influence of laser power on micropillars and superomniphobicity. (a) and (b) SEM images of LCE micropillars fabricated with laser power of 1 W and 6 W, respectively. (c) and (d) Contact angles and sliding angles, respectively, of water (blue) and hexadecane (red) on LCE micropillars fabricated with different laser powers, after surface modification with FDTCS. Insets in d represent wetting state of water (blue) and hexadecane (red) at 1 W and 6 W.

1200 cm^{-1} corresponding to –CF, $–CF_2$ and $–CF_3$ group stretching, and absorption peaks around 575 cm^{-1}, 730 cm^{-1} and 1120 cm^{-1} corresponding to vibration of the –C–F bond in –CF, $–CF_2$ and $–CF_3$ groups.[37,58] Our LCE-based superomniphobic surfaces were extremely repellent (with $\theta^* > 150^\circ$ and $\omega < 10^\circ$) for a wide range of liquids with surface tensions ranging from 72.1 mN m^{-1} to 27.5 mN m^{-1} (Fig. 5b and SI Section S5). Furthermore, to confirm the wetting state of our surfaces, we estimated the breakthrough pressure P_b (*i.e.*, the pressure at which the droplet transitions from the Cassie–Baxter state to the Wenzel state) and compared it with the applied Laplace pressure P_a (SI Section S6). Our results indicate that $P_b > P_a$ for both water and hexadecane on superomniphobic LCEs implying that the droplets adopted a stable Cassie–Baxter state only upon fluorination. This is also evident from the bouncing and sliding of water and hexadecane droplets on our LCE-based superomniphobic surfaces (Fig. 5c, d and Movie S1).

In this work, we selected liquid crystal elastomers (LCEs) as the responsive substrate because their nematic–isotropic transition enables reversible shape metamorphosis through programmable anisotropic strain.[59–62] In the aligned nematic state at room temperature (~25 °C), the spatially encoded director field dictates local deformation and defines the fabricated architectures including roll, twist, and flower geometries (Fig. 6a and experimental section). Upon heating to ~80 °C, the director field loses orientational order and the LCE transitions to the isotropic state (Fig. 6b). This order–disorder transition temporarily erases the programmed anisotropic strain gradients, driving pronounced shape reconfiguration to flat LCEs. Cooling restores the programmed nematic alignment and recovers the original programmed shapes, confirming reversible, thermally driven actuation (Fig. 6c–e). Furthermore, fluorination used to impart superomniphobicity did not compromise the intrinsic thermoresponsive behavior of the LCEs. The modified LCE surfaces retained robust actuation, mechanical integrity, and shape recovery over repeated heating–cooling cycles (Fig. 6f and SI Sections S7–S9). These results demonstrate that we successfully integrated superomniphobicity on LCE surface without degrading the reversible metamorphosis capabilities.

Furthermore, our LCE-based superomniphobic surfaces with reversible metamorphosis displayed resistance to corrosive substances, maintaining their integrity and performance (*i.e.*, reversible metamorphosis) when exposed to liquids with a wide range of pH values (acidic, neutral, and basic) as well as after immersion in water, concentrated acid (*e.g.*, sulfuric acid), concentrated base (*e.g.*, sodium hydroxide) and oxidizer (*e.g.*, 30% hydrogen peroxide) for 10 days (SI Section S10). In addition, our LCE-based superomniphobic surfaces also demonstrated the retention of superomniphobicity and reversible metamorphosis even after exposure to humid air (relative humidity ≈ 35%) for 10 days, exposure to 385 nm UV radiation for 120 min, as well as exposure to 10 000 water and hexadecane droplets sliding past the surface (SI Section S11). This dual functionality, *i.e.*, combination of reversible metamorphosis

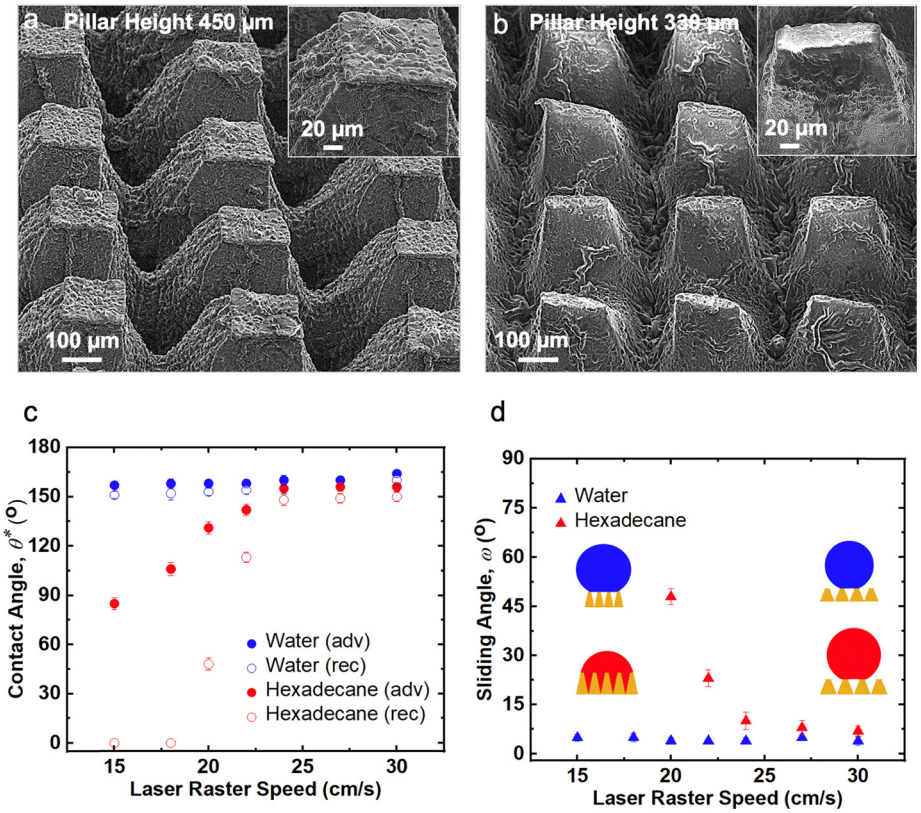

Fig. 4 Influence of raster speed on micropillars and superomniphobicity. (a) and (b) SEM images of LCE micropillars fabricated with laser raster speed of 24 cm s^{-1} and 15 cm s^{-1}, respectively. (c) and (d) Contact angles and sliding angles, respectively, of water (blue) and hexadecane (red) on LCE micropillars fabricated with different laser raster speeds, after surface modification with FDTCS. Insets in d represent wetting state of water and hexadecane at 15 cm s^{-1} and 24 cm s^{-1}.

and superomniphobicity, makes our LCE-based surfaces suitable for applications requiring shape change in harsh chemical environments.

Our LCE-based superomniphobic surfaces with reversible metamorphosis are suitable for loss-less droplet manipulation using a wide range of liquids. While metamorphosis of the LCE allows for droplet actuation in response to heat, the superomniphobicity allows for loss-less and rapid droplet manipulation with a wide range of liquids. To illustrate this, we designed an LCE-based superomniphobic surface that is curved upwards (See Experimental section). At room temperature (~25 °C), this LCE-based superomniphobic surface was in the nematic state, with the as-fabricated shape (Fig. 7a and e). At elevated temperature (~80 °C), the LCE-based superomniphobic surface transitioned to the isotropic state, resulting in flattening of the curved surface (Fig. 7b and f). To demonstrate the loss-less manipulation of droplets, we placed two 20 μL colored water droplets (blue) close to the free ends of the flattened LCE-based superomniphobic surface at 80 °C. The sliding angle (ω), which dictates droplet mobility, defines the minimum surface tilt required for a droplet to overcome interfacial adhesion (SI Section 12). Upon cooling under ambient conditions, the LCE-based superomniphobic surface gradually transitioned back to the nematic state, and as result it gradually curved upwards (Fig. 7c and g). When the tilt angle of curved LCE-based superomniphobic surface exceeded the sliding angle (ω = 4° for water), the water droplets rolled from the free ends towards the center and mixed with each other (Fig. 7d and h and Movie S2). This rolling and mixing of droplets demonstrate the potential for temperature-controlled droplet manipulation on LCE-based superomniphobic surfaces for chemical reactions. To demonstrate the chemical reaction, we placed a 20 μL droplet of sodium hydroxide solution (NaOH, colorless) and a 20 μL droplet of ferric chloride solution ($FeCl_3$, yellow) close to the free ends of the flattened LCE-based superomniphobic surface at 80 °C (Fig. 7j). Upon cooling under ambient conditions, the droplets rolled from the free ends towards the center and mixed with each other, producing a distinct color change due to the formation of ferric hydroxide (brown, $Fe(OH)_3$; Fig. 7k and l and Movie S3). In addition to aqueous liquids (with high surface tension), superomniphobic surfaces enable manipulation of organic liquids (with low surface tension). To demonstrate the manipulation of organic liquids, we placed two 20 μL droplets of hexadecane (red) close to the free ends of the flattened LCE-based superomniphobic surface at 80 °C (Fig. 7n). Upon cooling under ambient conditions, when the tilt angle of curved LCE-based superomniphobic surface exceeded the roll off angle (ω = 8° for hexadecane), the hexadecane droplets rolled from the free ends towards the center and mixed with each other (Fig. 7o and p and Movie S4).

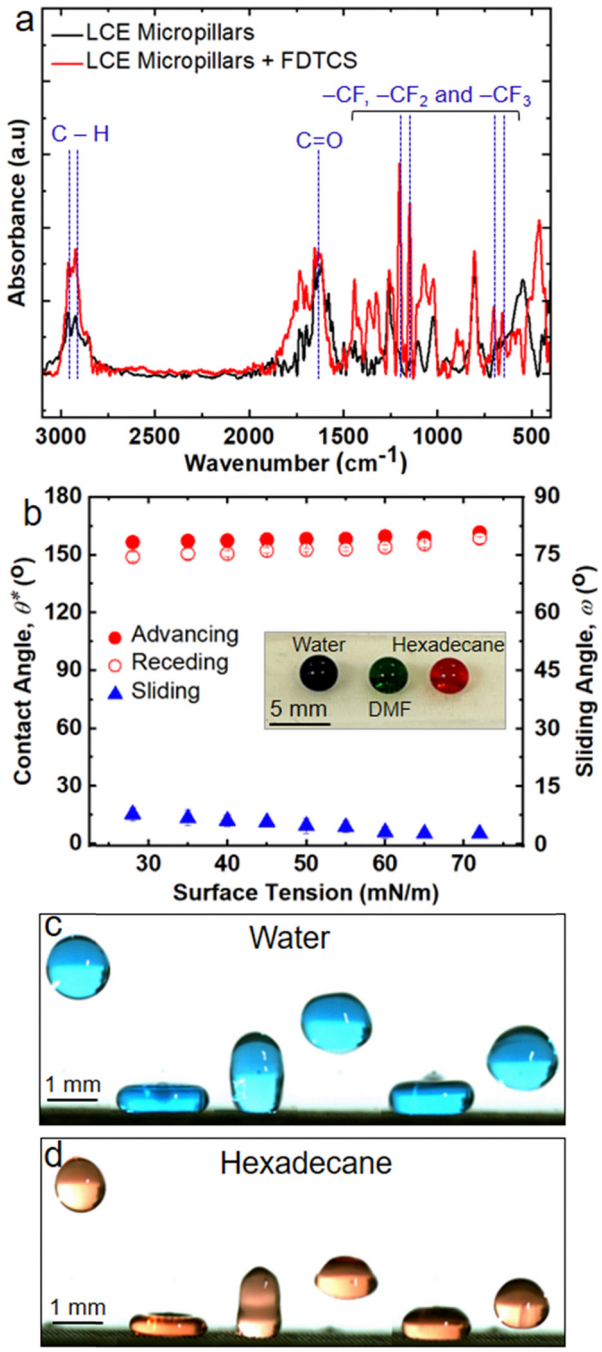

Fig. 5 Characterization of liquid repellency of LCE-based superomniphobic surfaces. (a) FTIR spectra of LCE micropillars before (black) and after (red) modification with FDTCS. (b) Contact angles and sliding angles for a wide range of liquids with surface tensions ranging from water (γ_{lv} =72.1 mN m^{-1}) to hexadecane (γ_{lv} = 27.5 mN m^{-1}) on LCE-based superomniphobic surfaces. Inset shows droplets of water (blue), *N*,*N*-dimethylformamide (DMF, green) and hexadecane (red) beading up on LCE-based superomniphobic surfaces. (c) and (d) Snapshots depicting bouncing droplets of water (blue) and hexadecane (red), respectively, on LCE-based superomniphobic surfaces.

Such loss-less droplet manipulation using LCE-based superomniphobic surfaces is attractive for open-channel microfluidic devices (*e.g.*, on–off gating). To accomplish this, we fabricated open-channel microfluidic devices (two chambers and a connecting channel) with LCE-based superomniphobic surfaces (see Experimental section). At room temperature, when the device is tilted, and liquid droplets are placed in the upper chamber, the droplets would immediately roll off and transport through the connecting channel into the lower chamber (*i.e.*, the "on" state; Fig. 7q). However, at an elevated temperature (~80 °C), the connecting channel shrinks due to nematic–isotropic transition, and restricts entry of liquid droplets (*i.e.*, the "off" state; Fig. 7r). To demonstrate this selective droplet transport *via* on–off gating, at room temperature (~25 °C), we tilted the device by 10° and placed water droplets (blue) in the upper chamber, and they immediately rolled off and transported through the connecting channel into the lower chamber (Fig. 7s). However, at an elevated temperature (~80 °C), the connecting channel shrank and restricted the entry of water droplets (Fig. 7t and Movie S5). Such on–off gating with LCE-based superomniphobic surfaces is attractive for selective and controlled chemical reactions. To demonstrate this, at room temperature (~25 °C), on a tilted device, we placed a $FeCl_3$ droplet (yellow) in the upper chamber, and it immediately rolled off and transported through the connecting channel into the lower chamber (Fig. 7u). Subsequently, we placed a NaOH droplet (colorless) in the upper chamber, and it also immediately rolled off and transported through the connecting channel into the lower chamber and mixed with the $FeCl_3$ droplet to form $Fe(OH)_3$ (brown, Fig. 7u). However, at an elevated temperature (~80 °C), the connecting channel shrank and restricted the entry of the NaOH droplet, preventing the chemical reaction (Fig. 7v and Movie S6). Such loss-less droplet manipulation cannot be achieved without superomniphobicity (SI Section 13). Therefore, the reversible metamorphic behavior of LCE-based superomniphobic surfaces have the potential for a wide range of applications including microfluidic reactors, lab-on-chip technologies, adaptive liquid-handling devices, controlled drug delivery systems *etc.*

3. Conclusion

In summary, we fabricated reversible metamorphic superomniphobic surfaces using simple, inexpensive, scalable, and solvent-free CO_2 laser engraving on LCEs, followed by surface modification to impart low solid surface energy. To obtain the appropriate surface texture necessary for superomniphobicity, we investigated the influence of laser power and laser raster speed on the surface texture and surface wettability. Using our LCE-based superomniphobic surfaces, we demonstrated loss-less manipulation of liquid droplets, mixing, selective chemical reaction, and open-channel microfluidic on–off gating for a wide range of liquids, including both high and low surface tension liquids. We also demonstrated the reversible metamorphic property of our LCE-based superomniphobic surfaces remains intact when exposed to liquids with a wide range of pH values and harsh chemical conditions. Our LCE-based superomniphobic surfaces retain superomniphobicity against harsh liquids, environmental conditions and minor solid abrasions such as touch (Movie S7) and knife scratching (Movie S8).

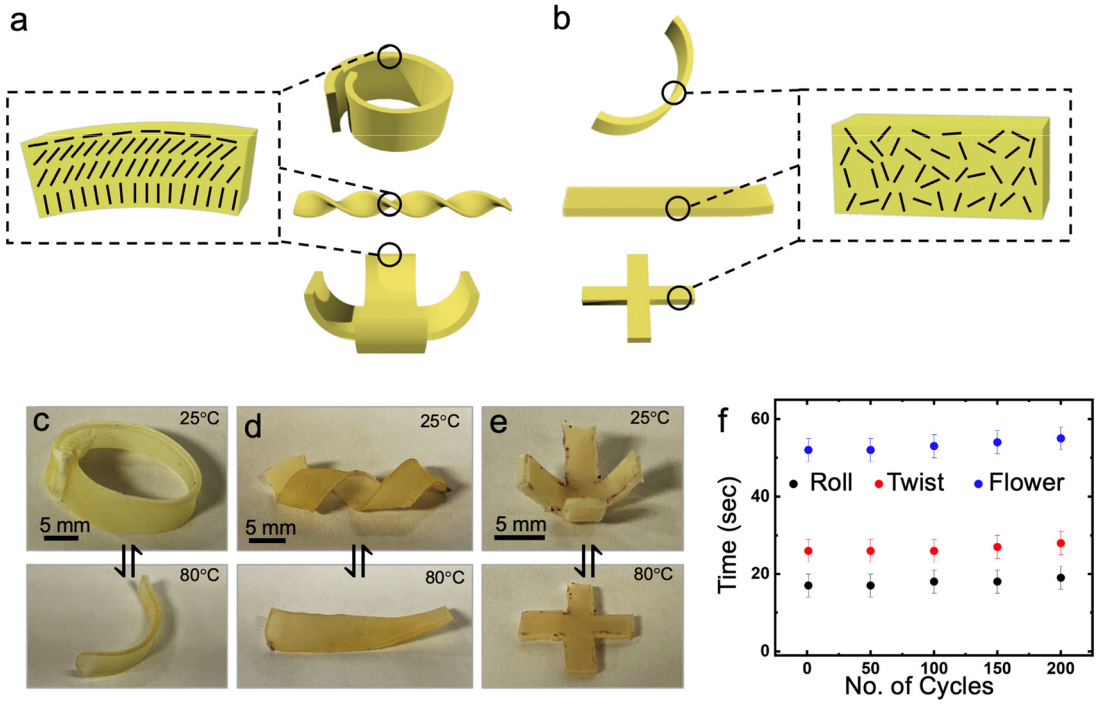

Fig. 6 Reversible metamorphosis of LCE-based superomniphobic surfaces. Schematic depicting spatially encoded director fields on roll, twist and flower shaped LCEs at (a) nematic state, and (b) isotropic state. Images displaying the reversible actuation of LCE-based superomniphobic surfaces with – (c) roll, (c) twist and (d) flower shapes. (e) Actuation response time superomniphobic LCE shapes.

Further efforts are required to improve their durability against major solid abrasion. We envision that our LCE-based superomniphobic surfaces with reversible metamorphosis will pave the way towards a wide range of applications including microfluidic reactors, lab-on-chip technologies, adaptive liquid-handling devices, controlled drug delivery systems, and anti-fouling coatings marking a promising direction for future research and development in materials science.

4. Experimental section

Fabrication of liquid crystal elastomers (LCEs)

To fabricate liquid crystal elastomers (LCEs), we added 1 g of 4-bis-[4-(3-acryloyloxypropypropyloxy) benzoyloxy]-2-methylbenzene (RM257; Fisher) into a glass vial. RM257 is a di-acrylate mesogen and is received as a powder. To dissolve the RM257, we added 0.4 g of toluene (Fisher) and heated the mixture to 80 °C on a hot plate (Fisher). Once the RM257 was dissolved, the solution was cooled to room temperature. Next, we added 0.21 g of 2,2-(ethylenedioxy) diethanethiol (EDDET; Sigma), a dithiol monomer and 0.05 g of pentaerythritol tetrakis(3-mercaptopropionate) (PETMP; Fisher), a tetrafunctional thiol crosslinker. Subsequently, we added 0.006 g of (2-hydroxyethoxy)-2-methylpropiophenone (HHMP; Sigma), a photoinitiator facilitating the secondary photopolymerization stage. In parallel, we prepared a catalyst solution by diluting dipropylamine (DPA; Sigma) with toluene at a ratio of 1 : 50, then we added 0.144 g of this diluted catalyst solution to the monomer solution and mixed vigorously on a Vortex mixer (Fisher). The monomer solution was degassed in a vacuum oven (Across International) for 1 min to remove any entrapped air bubbles from the mixing process. Then, the mixture was transferred into the desired mold, allowing the polymerization reaction to proceed for 12 h at ambient conditions. Next, the samples were placed in a vacuum oven at 80 °C for 24 h to ensure evaporation of the toluene. After evaporation of toluene, the resulting LCE samples exhibited a glossy, white, and opaque appearance at room temperature. This is a representation of the polydomain structure formed *via* Michael addition reaction with a uniform crosslink density. In order to fabricate monodomain LCEs, the polydomain LCE samples were stretched by ~100% strain to orient the mesogens in the desired direction, followed by exposure to 265 nm UV (UVP) to cross-link the residual acrylate groups resulting in a transparent nematic monodomain structure with locked director orientation. For roll and twist geometries, the polydomain films were stretched and wrapped around cylindrical tubes and crosslinked under 265 nm UV to form monodomain LCEs with locked director orientation. To create flower-shaped actuators, we cut an "X-shaped" template from the polydomain film, individually stretched each leaflet to define its local director alignment, and crosslinked under 265 nm UV to form monodomain LCEs with locked director orientation. The resulting shapes exhibited a reversible metamorphic property in response to change in temperature.

Fabrication of reversible metamorphic superomniphobic surfaces *via* laser ablation and surface modification

The laser ablation of LCEs was performed using an inexpensive, simple, scalable, solvent-free and commercially available CO_2

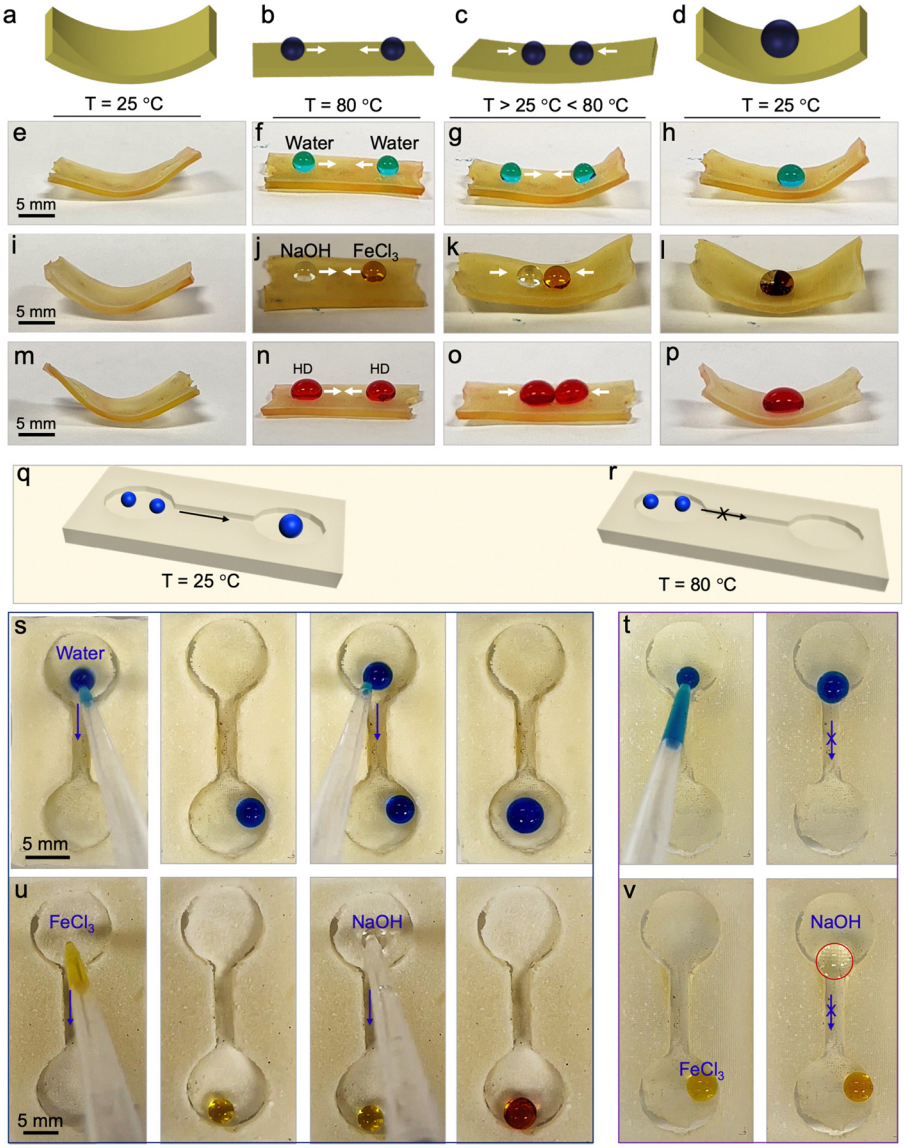

Fig. 7 Reversible metamorphosis for loss-less droplet manipulation, merging, mixing and chemical reaction. Schematics depicting the actuation and droplet merging on an LCE-based superomniphobic surface at different temperatures (T) – (a) 25 °C, (b) 80 °C, (c) 25 °C < T < 80 °C, and (d) 25 °C. (e–h) Loss-less manipulation, merging and mixing of two water droplets (blue). (i–l) Loss-less manipulation, merging, mixing and chemical reaction of a droplet of NaOH (colorless) with a droplet of $FeCl_3$ (yellow), resulting in $Fe(OH)_3$ (brown). (m–p) Loss-less manipulation, merging and mixing of two hexadecane droplets (red). (q) and (r) Schematics depicting the "on" and "off" states, respectively, of the open-channel microfluidic gating device for selective mixing and chemical reaction. (s) Water droplets (blue) transporting through the connecting channel in the "on" state at 25 °C. (t) Water droplets (blue) unable to transport through the connecting channel in the "off" state at 80 °C. (u) NaOH droplet (colorless) transporting through the connecting channel and merging with the $FeCl_3$ droplet (yellow) in the "on" state at 25 °C, resulting in $Fe(OH)_3$ (brown). (v) NaOH droplet (colorless) unable to transport through the connecting channel in the "off" state at 80 °C, preventing the chemical reaction.

laser (Universal Laser VLS 6.60T) with a central wavelength of 9.5 μm. The laser ablation was conducted over the LCE surfaces with different powers up to 12 W and different laser raster speeds up to 29 cm s^{-1}, at a fixed pulses per inch (PPI) of 500. After laser texturing, the LCE surfaces were subjected to hydroxylation in an oxygen plasma chamber under controlled conditions of 10 psi oxygen pressure, 20 cc min^{-1} oxygen flow rate, and 30 W plasma power for 20 min. Following the plasma treatment, the hydroxylated surfaces were modified through vapor-phase silanization at 120 °C for 1 hour using 200 μL of heptadecafluoro-1,1,2,2-tetrahydrodecyl trichlorosilane (Gelest) to impart low solid surface energy ($\gamma_{sv} \approx 10$ mN m^{-1}). The combination of low solid surface energy and re-entrant texture resulted in the reversible metamorphic superomniphobic surfaces.

Fabrication of microfluidic devices

To design a microfluidic device for selective droplet mixing *via* on–off gating, we first fabricated a positive replica of the microfluidic device shape using a 3D printer (Elegoo). Next,

the liquid crystal elastomer (LCE) solution was poured on the positive replica and allowed to crosslink for 12 h at room temperature. Then, laser ablation was performed on the LCE-based microfluidic device to create re-entrant texture, followed by vapor-phase fluorination to impart low solid surface energy, following the aforementioned method.

Contact angle and sliding angle measurements

Contact angles and sliding angles of different liquids were measured using a goniometer (Ramé-Hart 260-F4). A series of liquids with varying surface tensions were prepared by adding ethanol (Fisher) in water. Contact angles were measured by advancing or receding a small volume of liquid ($\sim$20 μL) onto the surface using a micrometer syringe (Gilmont). Sliding angles were measured by slowly tilting the stage until the droplet ($\sim$20 μL) rolled off from the surface. All results are the average of three individual measurements.

Morphology characterization

Surface morphology was characterized using a scanning electron microscope (SEM; Thermofisher Phenom Pharos) at 2 kV with a secondary electron detector. The samples were sputter coated with a thin film of gold prior to imaging (Cressington 108). Depth profiles were obtained using a confocal laser scanning microscope (Keyence VKx1100).

Structural characterization

Structural organization of polydomain and monodomain LCEs was characterized using polarized light microscope (Nikon Eclipse 50i POL). Polarized interference images were obtained using a 530 nm P-Cl filter (Nikon, Japan)

FTIR characterization

Samples for FTIR (Thermo Scientific Nicolet iS50) were prepared by mixing the desired material with KBr powder to form a pellet. Samples were analyzed with DTGS/KBr detector, and spectra were recorded at 2 cm^{-1} resolution with 32 scans. Background spectra were obtained with an empty pellet holder.

Mechanical characterization

The quasi-static mechanical properties were measured using ASTM Type I specimens in a tensile tester (Instron).[63,64] Force was measured with a 2 kN load cell (Instron) and displacement was measured using the crosshead velocity (20 mm min^{-1}). Specimen dimensions were used to convert the force-displacement curves to stress–strain curves.

Droplet bouncing

Movies of colored water (methylene blue: 10 μg mL^{-1}) and hexadecane (Oil Red O: 10 μg mL^{-1}) droplets bouncing on the LCE-based superomniphobic surfaces were obtained using a high-speed camera (Fastcam Mini AX200) at 1000 frames per second.

Chemical resistance

To assess chemical resistance, our LCE-based superomniphobic surfaces were exposed to corrosive (*i.e.*, acidic and basic) liquids with a wide range of pH values ($1 < pH < 13$) for 1 h, and immersed in concentrated sulfuric acid, concentrated sodium hydroxide and 35% hydrogen peroxide for 10 days. Subsequently, we measured the contact angles and sliding angles of hexadecane to assess superomniphobicity.

Author contributions

A. K. K conceived the idea. A. M. R, S. P, A. N, Y. J. K, M. Z, and H. N conducted the experiments. A. M. R, S. P, A. N, Y. J. K, M. Z, and H. N and A. K. K. conducted the analysis. A. M. R, S. P, A. N, Y. J. K, M. Z, and H. N and A. K. K. wrote the manuscript. All authors have contributed significantly to the work reported in this paper. Each author has read and approved the final version of the manuscript prior to submission.

Conflicts of interest

The authors declare that they have no known competing financial interests or personal relationships that could have appeared to influence the work reported in this paper.

Data availability

The data that supports the findings of this study are available in the manuscript and from the corresponding author.

Supplementary information (SI) is available. See DOI: https://doi.org/10.1039/d5mh01295c.

Acknowledgements

A. K. K gratefully acknowledges financial support under award 2245427 from the National Science Foundation, under award R01HL166724 from the National Institutes of Health, and under award HT94252310663 from Congressionally Directed Medical Research Programs.

Notes and references

1 C. Ohm, M. Brehmer and R. Zentel, Liquid crystalline elastomers as actuators and sensors, *Adv. Mater.*, 2010, **22**(31), 3366–3387.
2 T. J. White and D. J. Broer, Programmable and adaptive mechanics with liquid crystal polymer networks and elastomers, *Nat. Mater.*, 2015, **14**(11), 1087–1098.
3 Z. Guan, L. Wang and J. Bae, Advances in 4D printing of liquid crystalline elastomers: materials, techniques, and applications, *Mater. Horiz.*, 2022, **9**(7), 1825–1849.
4 K. M. Herbert, H. E. Fowler, J. M. McCracken, K. R. Schlafmann, J. A. Koch and T. J. White, Synthesis and alignment of liquid crystalline elastomers, *Nat. Rev. Mater.*, 2022, **7**(1), 23–38.

5 M. Chen, M. Gao, L. Bai, H. Zheng, H. J. Qi and K. Zhou, Recent advances in 4D printing of liquid crystal elastomers, *Adv. Mater.*, 2023, **35**(23), 2209566.
6 Y. Zhang, Z. Wang, Y. Yang, Q. Chen, X. Qian, Y. Wu, H. Liang, Y. Xu, Y. Wei and Y. Ji, Seamless multimaterial 3D liquid-crystalline elastomer actuators for next-generation entirely soft robots, *Sci. Adv.*, 2020, **6**(9), eaay8606.
7 Y. Huang, Y. Xu, H. K. Bisoyi, Z. Liu, J. Wang, Y. Tao, T. Yang, S. Huang, H. Yang and Q. Li, Photocontrollable Elongation Actuation of Liquid Crystal Elastomer Films with Well-Defined Crease Structures, *Adv. Mater.*, 2023, **35**(36), 2304378.
8 S. Li, H. Bai, Z. Liu, X. Zhang, C. Huang, L. W. Wiesner, M. Silberstein and R. F. Shepherd, Digital light processing of liquid crystal elastomers for self-sensing artificial muscles, *Sci. Adv.*, 2021, **7**(30), eabg3677.
9 J. H. Lee, J. Bae, J. H. Hwang, M. Y. Choi, Y. S. Kim, S. Park, J. H. Na, D. G. Kim and S. K. Ahn, Robust and reprocessable artificial muscles based on liquid crystal elastomers with dynamic thiourea bonds, *Adv. Funct. Mater.*, 2022, **32**(13), 2110360.
10 Y. Xu, A. M. Rather, S. Song, J.-C. Fang, R. L. Dupont, U. I. Kara, Y. Chang, J. A. Paulson, R. Qin and X. Bao, Ultrasensitive and selective detection of SARS-CoV-2 using thermotropic liquid crystals and image-based machine learning, *Cell Rep. Phys. Sci.*, 2020, **1**, 12.
11 J. Jiang and Y. Zhao, Liquid crystalline elastomer for separate or collective sensing and actuation functions, *Small*, 2023, **19**(34), 2301932.
12 Y. Yu and T. Ikeda, Soft actuators based on liquid-crystalline elastomers, *Angew. Chem., Int. Ed.*, 2006, **45**(33), 5416–5419.
13 Y. Zhao, Y. Chi, Y. Hong, Y. Li, S. Yang and J. Yin, Twisting for soft intelligent autonomous robot in unstructured environments, *Proc. Natl. Acad. Sci. U. S. A.*, 2022, **119**(22), e2200265119.
14 Y. Xu, A. M. Rather, Y. Yao, J.-C. Fang, R. S. Mamtani, R. K. Bennett, R. G. Atta, S. Adera, U. Tkalec and X. Wang, Liquid crystal–based open surface microfluidics manipulate liquid mobility and chemical composition on demand, *Sci. Adv.*, 2021, **7**(40), eabi7607.
15 A. J. Kragt, D. J. Broer and A. P. Schenning, Easily processable and programmable responsive semi-interpenetrating liquid crystalline polymer network coatings with changing reflectivities and surface topographies, *Adv. Funct. Mater.*, 2018, **28**(6), 1704756.
16 Z. L. Wu, A. Buguin, H. Yang, J. M. Taulemesse, N. Le Moigne, A. Bergeret, X. Wang and P. Keller, Microstructured nematic liquid crystalline elastomer surfaces with switchable wetting properties, *Adv. Funct. Mater.*, 2013, **23**(24), 3070–3076.
17 H. Shahsavan, S. M. Salili, A. Jákli and B. Zhao, Smart Muscle-Driven Self-Cleaning of Biomimetic Microstructures from Liquid Crystal Elastomers, *Adv. Mater.*, 2015, **27**(43), 6828–6833.
18 Y. Zhan, J. Zhao, W. Liu, B. Yang, J. Wei and Y. Yu, Biomimetic submicroarrayed cross-linked liquid crystal polymer films with different wettability via colloidal lithography, *ACS Appl. Mater. Interfaces*, 2015, **7**(45), 25522–25528.
19 Y. Liu, C. Zhu, Y. Zhao, X. Qing, F. Wang, D. Deng, J. Wei and Y. Yu, Directed pinning of moving water droplets on photoresponsive liquid crystal mats, *Adv. Mater. Interfaces*, 2019, **6**(21), 1901158.
20 F. Ge and Y. Zhao, Microstructured actuation of liquid crystal polymer networks, *Adv. Funct. Mater.*, 2020, **30**(2), 1901890.
21 Y. Li, Y. Teixeira, G. Parlato, J. Grace, F. Wang, B. D. Huey and X. Wang, Three-dimensional thermochromic liquid crystal elastomer structures with reversible shape-morphing and color-changing capabilities for soft robotics, *Soft Matter*, 2022, **18**(36), 6857–6867.
22 M. Bobnar, N. Derets, S. Umerova, V. Domenici, N. Novak, M. Lavrič, G. Cordoyiannis, B. Zalar and A. Rešetič, Polymer-dispersed liquid crystal elastomers as moldable shape-programmable material, *Nat. Commun.*, 2023, **14**(1), 764.
23 A. Rešetič, Shape programming of liquid crystal elastomers, *Commun. Chem.*, 2024, **7**(1), 56.
24 T. Young, III. An essay on the cohesion of fluids, *Philos. Trans. R. Soc. London*, 1805, **95**, 65–87.
25 R. N. Wenzel, Resistance of solid surfaces to wetting by water, *Ind. Eng. Chem.*, 1936, **28**(8), 988–994.
26 A. Cassie and S. Baxter, Wettability of porous surfaces, *Trans. Faraday Soc.*, 1944, **40**, 546–551.
27 Z. Chu and S. Seeger, Superamphiphobic surfaces, *Chem. Soc. Rev.*, 2014, **43**(8), 2784–2798.
28 A. K. Kota, Y. Li, J. M. Mabry and A. Tuteja, *Hierarchically structured superoleophobic surfaces with ultralow contact angle hysteresis*, 2012.
29 A. Lafuma and D. Quéré, Superhydrophobic states, *Nat. Mater.*, 2003, **2**(7), 457–460.
30 S. Movafaghi, S. Vallabhuneni, W. Wang, S. Jathar and A. K. Kota, Rapid and Onsite Detection of Fuel Adulteration, *Langmuir*, 2023, **39**(26), 9044–9050.
31 C. Furmidge, Studies at phase interfaces. I. The sliding of liquid drops on solid surfaces and a theory for spray retention, *J. Colloid Sci.*, 1962, **17**(4), 309–324.
32 W. Wang, K. Lockwood, L. M. Boyd, M. D. Davidson, S. Movafaghi, H. Vahabi, S. R. Khetani and A. K. Kota, Superhydrophobic coatings with edible materials, *ACS Appl. Mater. Interfaces*, 2016, **8**(29), 18664–18668.
33 S. Vallabhuneni, S. Movafaghi, W. Wang and A. K. Kota, Superhydrophobic coatings for improved performance of electrical insulators, *Macromol. Mater. Eng.*, 2018, **303**(9), 1800313.
34 H. Vahabi, W. Wang, K. C. Popat, G. Kwon, T. B. Holland and A. K. Kota, Metallic superhydrophobic surfaces via thermal sensitization, *Appl. Phys. Lett.*, 2017, **110**, 25.
35 A. M. Rather and U. Manna, Facile synthesis of tunable and durable bulk superhydrophobic material from amine ''reactive'' polymeric gel, *Chem. Mater.*, 2016, **28**(23), 8689–8699.
36 A. K. Kota, W. Choi and A. Tuteja, Superomniphobic surfaces: Design and durability, *MRS Bull.*, 2013, **38**(5), 383–390.
37 A. M. Rather, S. Vallabhuneni, A. J. Pyrch, M. Barrubeeah, S. Pillai, A. Taassob, F. N. Castellano and A. K. Kota, Color morphing surfaces with effective chemical shielding, *Nat. Commun.*, 2024, **15**(1), 3735.
38 W. Wang, H. Vahabi, S. Movafaghi and A. K. Kota, Superomniphobic surfaces with improved mechanical durability:

Synergy of hierarchical texture and mechanical interlocking, *Adv. Mater. Interfaces*, 2019, **6**(18), 1900538.
39 S. Movafaghi, W. Wang, A. Metzger, D. Williams, J. Williams and A. Kota, Tunable superomniphobic surfaces for sorting droplets by surface tension, *Lab Chip*, 2016, **16**(17), 3204–3209.
40 A. Tuteja, W. Choi, M. Ma, J. M. Mabry, S. A. Mazzella, G. C. Rutledge, G. H. McKinley and R. E. Cohen, Designing superoleophobic surfaces, *Science*, 2007, **318**(5856), 1618–1622.
41 H. Vahabi, W. Wang, S. Movafaghi and A. K. Kota, Free-standing, flexible, superomniphobic films, *ACS Appl. Mater. Interfaces*, 2016, **8**(34), 21962–21967.
42 A. K. Kota, G. Kwon and A. Tuteja, The design and applications of superomniphobic surfaces, *NPG Asia Mater.*, 2014, **6**(7), e109–e109.
43 W. Wang, J. Salazar, H. Vahabi, A. Joshi-Imre, W. E. Voit and A. K. Kota, Metamorphic superomniphobic surfaces, *Adv. Mater.*, 2017, **29**(27), 1700295.
44 J. Lee, Y. Guo, Y.-J. Choi, S. Jung, D. Seol, S. Choi, J.-H. Kim, Y. Kim, K.-U. Jeong and S.-K. Ahn, Mechanically programmed 2D and 3D liquid crystal elastomers at macro- and microscale via two-step photocrosslinking, *Soft Matter*, 2020, **16**(11), 2695–2705.
45 M. O. Saed, A. H. Torbati, D. P. Nair and C. M. Yakacki, Synthesis of programmable main-chain liquid-crystalline elastomers using a two-stage thiol-acrylate reaction, *J. Visualized Exp.*, 2016, **107**, e53546.
46 H. Q. Wang, Y. Tang, Z. Y. Huang, F. Z. Wang, P. F. Qiu, X. Zhang, C. H. Li and Q. Li, A Dual-Responsive Liquid Crystal Elastomer for Multi-Level Encryption and Transient Information Display, *Angew. Chem.*, 2023, **135**(48), e202313728.
47 D. R. Merkel, N. A. Traugutt, R. Visvanathan, C. M. Yakacki and C. P. Frick, Thermomechanical properties of monodomain nematic main-chain liquid crystal elastomers, *Soft Matter*, 2018, **14**(29), 6024–6036.
48 H. Liang, Y. Zhang, E. He, Y. Yang, Y. Liu, H. Xu, Z. Yang, Y. Wang, Y. Wei and Y. Ji, ''Cloth-to-Clothes-Like'' Fabrication of Soft Actuators, *Adv. Mater.*, 2024, **36**(29), 2400286.
49 Y. Takezawa, N. Furukawa, S. Nachimuthu, R. Zhou and A. Torbati, Higher-Order Structural Analysis of a Transparent and Flexible High Thermal Conductive Liquid Crystalline Elastomer Sheet and Its Composite, *ACS Omega*, 2024, **9**(19), 20839–20848.
50 A. Rešetič, J. Milavec, B. Zupančič, V. Domenici and B. Zalar, Polymer-dispersed liquid crystal elastomers, *Nat. Commun.*, 2016, **7**(1), 13140.
51 T. H. Ware, M. E. McConney, J. J. Wie, V. P. Tondiglia and T. J. White, Voxelated liquid crystal elastomers, *Science*, 2015, **347**(6225), 982–984.
52 A. F. Obilor, M. Pacella, A. Wilson and V. V. Silberschmidt, Micro-texturing of polymer surfaces using lasers: a review, *Int. J. Adv. Des. Manuf. Technol.*, 2022, **120**(1), 103–135.
53 R. T. Mushtaq, Y. Wang, M. Rehman, A. M. Khan and M. Mia, State-Of-The-Art and Trends in CO2 Laser Cutting of Polymeric Materials—A Review, *Materials*, 2020, **13**(17), 3839.
54 E. G. Gamaly, S. Juodkazis, K. Nishimura, H. Misawa, B. Luther-Davies, L. Hallo, P. Nicolai and V. T. Tikhonchuk, Laser-matter interaction in the bulk of a transparent solid: Confined microexplosion and void formation, *Phys. Rev. B: Condens. Matter Mater. Phys.*, 2006, **73**(21), 214101.
55 S. Ravi-Kumar, B. Lies, X. Zhang, H. Lyu and H. Qin, Laser ablation of polymers: a review, *Polym. Int.*, 2019, **68**(8), 1391–1401.
56 T. Lippert and J. T. Dickinson, Chemical and spectroscopic aspects of polymer ablation: Special features and novel directions, *Chem. Rev.*, 2003, **103**(2), 453–486.
57 T. Lippert, Interaction of Photons with Polymers: From Surface Modification to Ablation, *Plasma Processes Polym.*, 2005, **2**(7), 525–546.
58 J.-D. Brassard, D. K. Sarkar and J. Perron, Synthesis of monodisperse fluorinated silica nanoparticles and their superhydrophobic thin films, *ACS Appl. Mater. Interfaces*, 2011, **3**(9), 3583–3588.
59 Y. Wu, Y. Yang, X. Qian, Q. Chen, Y. Wei and Y. Ji, Liquid-crystalline soft actuators with switchable thermal reprogrammability, *Angew. Chem.*, 2020, **132**(12), 4808–4814.
60 L. Yin, L. Han, F. Ge, X. Tong, W. Zhang, A. Soldera and Y. Zhao, A Novel Side-Chain Liquid Crystal Elastomer Exhibiting Anomalous Reversible Shape Change, *Angew. Chem.*, 2020, **132**(35), 15241–15246.
61 G. Chen, B. Jin, Y. Shi, Q. Zhao, Y. Shen and T. Xie, Rapidly and Repeatedly Reprogrammable Liquid Crystalline Elastomer via a Shape Memory Mechanism, *Adv. Mater.*, 2022, **34**(21), 2201679.
62 H. Kim, J. Gibson, J. Maeng, M. O. Saed, K. Pimentel, R. T. Rihani, J. J. Pancrazio, S. V. Georgakopoulos and T. H. Ware, Responsive, 3D Electronics Enabled by Liquid Crystal Elastomer Substrates, *ACS Appl. Mater. Interfaces*, 2019, **11**(21), 19506–19513.
63 A. L. Gershon, A. K. Kota and H. A. Bruck, Characterization of quasi-static mechanical properties of polymer nanocomposites using a new combinatorial approach, *J. Compos. Mater.*, 2009, **43**(22), 2587–2598.
64 A. L. Gershon, D. P. Cole, A. K. Kota and H. A. Bruck, Nanomechanical characterization of dispersion and its effects in nano-enhanced polymers and polymer composites, *J. Mater. Sci.*, 2010, **45**, 6353–6364.